Materials Transactions

MT-M2023174

"Effect of Cooling Rate on Powder Characteristics and Microstructural Evolution of Gas Atomized β-Solidifying γ-TiAl Alloy Powder"
Sung-Hyun Park, Ryosuke Ozasa, Ozkan Gokcekaya, Ken Cho, Hiroyuki Y. Yasuda, Myung-Hoon Oh, Young-Won Kim and Takayoshi Nakano
Doi: https://doi.org/10.2320/matertrans.MT-M2023174

Received: October 24, 2023
Accepted: November 21, 2023
Published: December 15, 2023

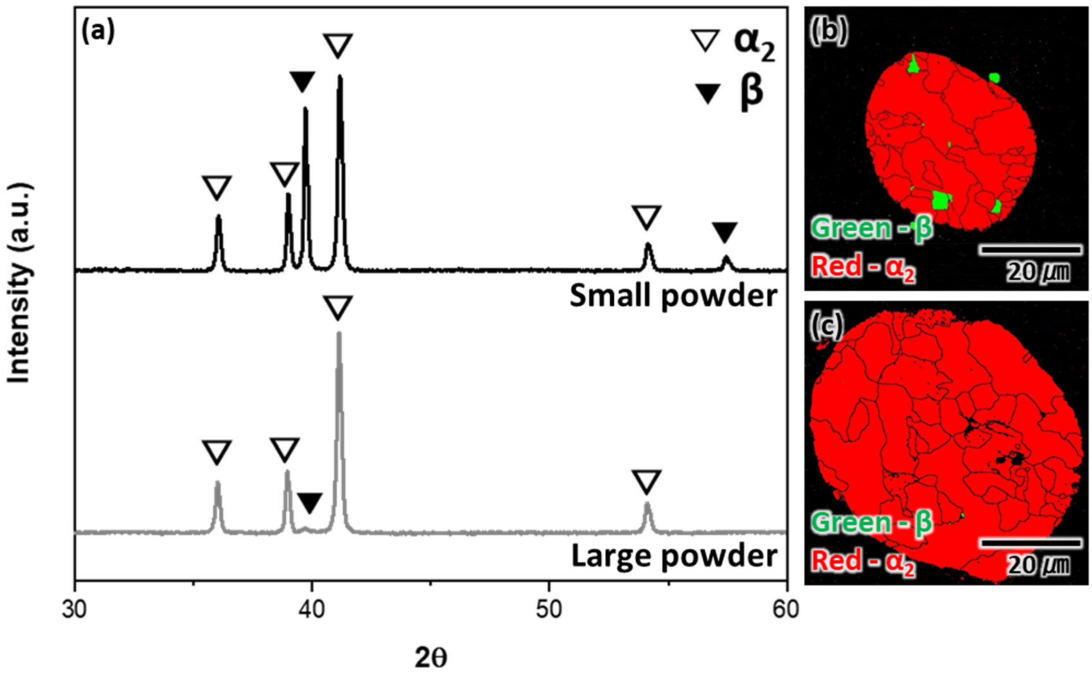

Graphical Abstract

Effect of Cooling Rate on Powder Characteristics and Microstructural Evolution of Gas Atomized β-Solidifying γ-TiAl Alloy Powder

Sung-Hyun Park[1], Ryosuke Ozasa[1,2], Ozkan Gokcekaya[1,2], Ken Cho[1,2], Hiroyuki Y. Yasuda[1,2], Myung-Hoon Oh[3], Young-Won Kim[4], Takayoshi Nakano[1,2,*]

[1] Division of Materials and Manufacturing Science, Graduate School of Engineering, Osaka University, 2-1, Yamadaoka, Suita, Osaka 565-0871, Japan

[2] Anisotropic Design & Additive Manufacturing Research Center, Osaka University, 2-1, Yamadaoka, Suita, Osaka 565-0871, Japan

[3] School of Materials Science and Engineering, Kumoh National Institute of Technology (KIT), 61 Daehakro, Gumi, Gyeongbuk, 39177, Republic of Korea

[4] Gamteck LLC, Dayton, OH, 45431, USA

*Corresponding author:
Prof. Dr. Takayoshi Nakano
Division of Materials and Manufacturing Science
Graduate School of Engineering, Osaka University
2-1 Yamadaoka, Suita, Osaka 565-0871, Japan
Tel.: +81-6-6879-7505; Fax: +81-6-6879-7505
E-mail: nakano@mat.eng.osaka-u.ac.jp

Abstract

The gas atomization is a production technique of a metallic powder. In this study, the β-solidifying Ti-44Al-6Nb-1.2Cr alloy powder fabricated by gas-atomization was investigated regarding the evolving shape, phase constitution, and chemical distribution as a result of the high solidification rate. The powder showed a spherical shape regardless of its size, indicating no relation of solidification rate to powder shape. However, the small powder (D_{50} = 36.0 μm) showed less segregation and was composed of β and α_2 dual phases. Whereas, the large powder (D_{50} = 78.7 μm) is relatively high segregation and composed of almost a single α_2 phase because of the difference in the cooling rates. The findings obtained here demonstrated the understanding of phase transformation during the rapid solidification and continuous microstructural evolution process in the β-solidifying alloy.

Keywords: gas atomization; segregation; rapid solidification; γ-TiAl alloy; phase transformation

1. Introduction

Recently, the transportation industry has been required to develop advanced structural materials to reduce environmental impact and improve energy performance.[1] Among the various structural materials, γ-Titanium aluminide (γ-TiAl) alloys are attractive candidates for high-temperature applications with their low density and excellent mechanical properties.[2,3] Because of the cost efficiency, the γ-TiAl alloy parts are generally produced by the investment casting process. However, this methodology is difficult to fabricate complex shapes, and the microstructural inhomogeneities lead to the variability of the mechanical properties.[4,5] Thus, powder metallurgy has raised interest because of its comparative advantages, which promise a more fine and homogeneous microstructure, reducing the unnecessary additional processing through near-net shape, and enhancement of the mechanical properties by establishing peculiar microstructure such as additive manufacturing (AM) process.[5-11]

Gas-atomization is a widely adopted manufacturing process for the production of various metallic powders.[12–14] Although the gas-atomization process demands more cost investment, it yields much better spherical particles.[15] The high sphericity of powder is attributed to the flowability of powder, ensuring high densification of the final product in the AM process.[16,17] On the other hand, the cooling rate during the gas-atomization process is in the range of around 10^6 K/s in the argon atmosphere,[13] which represents an extremely high cooling rate compared to other manufacturing processes. Thus, the equilibrium phase transformation during the powder processing is suppressed. Indeed, the β-solidifying γ-TiAl alloys undergo numerous phase transformations during the solidification process. The phase transformation sequence is $L \rightarrow L + \beta \rightarrow \beta \rightarrow \alpha + \beta \rightarrow \alpha$ [18], the equilibrium microstructure consisted of a mixture of the α_2/γ colonies and a small amount of the γ, β grains.[18,19] However, the phase constitutions and morphology are strongly influenced by the cooling rate and sensitively changed. The gas-atomized β-solidifying γ-TiAl alloy powder contained the massively transformed α, α′ (disordered α) acicular γ′, and β phase owing to the high cooling rate.[20] In addition, even quenching from the β phase region represented distinctly different microstructural characteristics due to martensitic transformation.[21,22] It means the complex microstructural evolution and formation mechanisms in the non-equilibrium state of γ-TiAl alloys are still not fully understood. Thus, a comprehensive investigation is necessary to address phase transformation under the rapid solidification condition of the γ-TiAl alloys.

In this study, we focused on the influence of the high cooling rate on the powder characteristics. In particular, focus on microstructural evolution in β-solidifying γ-TiAl alloy. The two different sizes of the gas-atomized powder were investigated for their shape, chemical distribution, and phase constitution. Furthermore, we discussed the overall process of the microstructure development. Consequently, the results could refer to understanding the effect of cooling rate on microstructural evolution in β-solidifying γ-TiAl alloys, particularly under the rapid solidification condition.

2. Materials and methods

Gas-atomized Ti-44Al-6Nb-1.2Cr (at.%) alloy powder (Osaka titanium technologies, Japan) was used. The nominal composition of alloy powder was evaluated as Ti (balance), Al (43.77), Nb (5.96), and Cr (1.22) by inductively coupled plasma optical emission spectroscopy. The powders were classified into small and large powders by means of a sieving technique using the supplied powders. The compositional difference in Al content between the two groups of powders was less than 0.2 at.% because they were produced from the same lot of raw materials.

Particle size distribution was analyzed using a laser-diffraction-type particle size distribution measuring device (Mastersizer 3000E, Malvern Panalytical, UK), The powder samples were observed using field emission scanning electron microscopy (FE-SEM; JEM-6500F, JEOL, Japan), and the quantitative analysis of the particle shape was performed using a dynamic particle image analysis system (iSpect DIA-10, Shimadzu, Japan). Circularity was calculated by dividing the area equivalent diameter by the perimeter equivalent diameter.

Diffraction profiles were obtained using an X-ray diffractometer (XRD; X'pert PRO, PANalytical, Netherlands) for the phase identification of each powder. Each powder was embedded in acrylic resin (KM-CO, PRESI, France) and polished to a mirror finish. Thereafter, crystal phase distribution analysis was performed using electron backscatter diffraction (EBSD; NordlysMax^3, Oxford Instruments, UK). Elemental distribution analysis and the point analysis of composition were conducted using energy dispersive X-ray spectroscopy (EDS; X-Max^N, Oxford Instruments, UK).

3. Results and discussions

3.1 Influence of the cooling rate on powder characteristics

Although the gas atomization process represents high cooling rates, the difference in cooling rates depending on the powder size is identified, Thus, the observation groups were divided into small and large powders as shown in Fig. 1 because the expected cooling rate of each powder is approximately 4 $\times 10^{-5}$ K/s and 1 $\times$ 10^{-5} K/s, respectively. 13) Therefore, the characteristics of the powder are supposed to change with the particle size, and the particle size obtained here corresponds to the volume equivalent diameter. The detailed information is summarized in Table 1.

Fig. 2 shows the results of the particle size and shape analysis. The low magnification of FE-SEM images clearly shows the difference in average particle diameter between the small and large powders (Fig. 2(a,b)), which is consistent results with the particle size and distribution trends shown in Fig. 1. In terms of shape, particles relatively close to a spherical shape were observed in both powder groups. To quantitatively evaluate the particle shape, a two-dimensional projected image of the small powder was obtained as represented by Fig. 2(c). More detailed characteristics of the powder shape are shown in Table 2. It was found that the particles in the powder had high circularity (0.92 ± 0.6). Furthermore, the area equivalent diameter obtained from the particle image analysis (Fig. 2(d)) was less than 50 μm for most particles. In the relationship between the particle area equivalent diameter and circularity (Fig. 2(e)), the majority of particles had high circularity, regardless of the particle size, and no correlation ($R^2 = 0.03$, $p > 0.05$) between the particle diameter and circularity was observed. Therefore, the powders prepared by gas atomization contained particles that were close to a spherical shape regardless of the particle size, there was no noticeable difference in the powder shapes. Therefore, reasonable flowability and sufficient powder bed density can be expected, both powders are suitable for the AM process.

The metal AM process, especially the powder bed fusion (PBF) process can be divided into laser-PBF and electron beam-PBF depending on their heat source.[23) There are several different characteristics between the two process, different size of powders is recommended. [24) As an example, a smaller beam size of laser-PBF than electron beam-PBF results in deeper and narrow melt pools during the process. Therefore, to avoid defects caused by the lack of overlap of the melt pools and increase structural integrity, small powder is more suitable. On the other hand, explosive powder scattering, which is the so-called “smoking” phenomenon is one of the problems of the electron beam-PBF for manufacturing γ-TiAl alloys. One way of resolving this problem is using a large power[25), Thus, a larger powder is more suitable for the EB-PBF process.

However, a highly magnified FE-SEM image of the powder surface appearance exhibited dendritic morphology consisting of multi-nucleation (Fig.3(a)). This characteristic is consistently observed in similar-sized powders prepared in the gas-atomization methodology.[26,27) In the cross-section, the multi-nucleation gives rise to a concentric liquid/solid interface solidification geometry (Fig. 3(b)), wherein the dendrites showed gray contrast, while the interdendrites showed dark contrast, suggesting segregation of elements is likely.

Further detailed composition distribution was investigated for the small and large powders by EDS analysis. As shown in Fig. 4, there was a slight segregation of the constituent elements. Both powders indicated that Ti and Nb are richer in dendrite while Al and Cr are richer in inter-dendrite, which is similar results compared to the previous study.[28)] Since the distribution coefficient is greater than 1, the solute element tends to segregate in the dendrite. On the contrary, the solute element is discharged into the liquid phase resulting in segregation in the inter-dendrite when the distribution coefficient is less than 1. The calculated distribution coefficient of this alloy was 1.06 in Ti, 0.92 in Al, 1.11 in Nb, and 0.69 in Cr at the liquidus temperature, respectively. Compared to those exhibited by the large powder, the small powder suppressed elemental segregation because the small powder exposed a much higher cooling rate during the gas atomization process.[13] The elemental segregation can be successfully suppressed under rapid cooling conditions.[29,30]

In addition, XRD and SEM-EBSD analyses were conducted to confirm the constituent phase of the powders (Fig. 5). The small powder had confirmed diffraction peaks derived from the α_2 phase and the β phase. In contrast, the large powder consisting of a small amount of β phase showed predominant peaks derived from the α_2 phase. The determined phase volume fraction by SEM-EBSD were 8.3% of β phase, 91.7% of the α_2 phase in the small powder, and less than 0.5% of β phase, over 99.5% of the α_2 phase in the large powder, respectively. These changes in phase constitution depending on the particle size can be explained by the difference in the cooling rate. The composition of the investigated TiAl alloy in this study was Ti-44Al-6Nb-1.2Cr (at.%), which was proposed as a β-solidifying γ-TiAl alloy. The β-solidifying γ-TiAl alloy undergoes numerous phase transformations, and the transformation pathway is simply expressed as the liquid to β phase, β phase to $\alpha(\alpha_2)$ phase.[18]

Therefore, the fast cooling rate of the small size of the powder makes it difficult to provide enough time for phase transformation, resulting in the remaining of the primary β phase. On the other hand, the relatively slow cooling rate of the larger size of powder provides the time required for the phase transformation, exhibiting predominantly the α_2 phase microstructure. The proportion of β phase represented an increasing tendency as the particle size decreased which is consistent results with the previous study.[31)]

3.2 Microstructural evolution during the rapid solidification

Microstructural formation mechanisms for small and large powders can be inferred mainly related to the colling rate.

To figure out the chemical composition in the local area, further observation by SEM-EBSD and EDS was performed in the corresponding small size of powder (Fig 6). The image was not perfectly matched due to the image drifting.[32)] The results demonstrated the chemical composition near the interdendritic area with the α_2 phase (Point 1) was Ti (49.4), Al (43.4), Nb (6.0), Cr (1.2), whereas element distribution in the dendritic area with the β phase (Point 2) was Ti (50.4), Al (42.0), Nb (6.5), Cr (1.1), respectively. Namely, Ti and Nb were preferentially localized in dendrites whereas Al and Cr were localized in the inter-dendrite region, which is consistent results with the calculated distribution coefficient aforementioned. Thus, the segregation of elements is initiated when the solidification is initiated and can be expected to observe local chemical fluctuations during the rapid solidification process.

In terms of phase transformation, As illustrated in Fig.7(a) representing the findings of this study, the primary phase is the β phase during the solidification in the β-solidifying γ-TiAl alloy system. However, the nucleation of the primary β phase gradually increases the Al concentration in the liquid because of the distribution coefficient and the different diffusivity in the solid and liquid phases (Fig.7 (b)). The diffusivity in the solid is lower than in the liquid phase. The highly enriched

Al concentration was confirmed at the solid-liquid interface by the simulation during the rapid solidification.[33)], which indicated inter-dendrite regions as dark contrast in the FE-SEM image. After the solidification of β phase (Fig. 7(c)), the α phase started to transform directly from the solid β phase owing to a high cooling rate (Fig.7(d)). Furthermore, the nucleated α phase has blocky morphology with irregular grain boundaries because of the characteristic of the massive transformation Fig.7(c)).[20,34)] Thus, the microstructure investigated in the large size of the powder evolved. However, the still remaining β phase was observed in the small size of the powder because of the relatively higher cooling rate, and it is located on the outside of the powder where the cooling rate is higher within it. Lastly, among the various manufacturing methodologies, the AM process promises almost the same microstructural features demonstrated in this study because of the ultra-high cooling rate temperature fields and their repetitive thermal history during the process.[35] Therefore, the investigated microstructural evolution features in this study may have the potential to contribute to the understanding of microstructure characteristics in additively fabricated γ-TiAl alloys.

4. Conclusions

This study aimed to elucidate the effect of cooling rate on powder characteristics and microstructural evolution of the rapidly solidified β-solidifying γ-TiAl alloy. The following conclusions were drawn:

(1) A metallic powder produced by gas atomization contains particles with high circularity, regardless of particle size. However, the level of the segregation and powder contains different crystal phases depending on the particle size. The small powder, with a high solidification rate, relatively suppressed segregation and had β and α_2 phases, while the large powder, with a low solidification rate, represented distinct segregation and consisted of an almost α_2 phase.

(2) The local elemental deviations were observed during the solidification process, especially, Al composition highly concentrated at the solid-liquid interface. In addition, the massive type of $\alpha(\alpha_2)$ phase transformation was identified instead of the β and α phase separation due to rapid solidification.

These findings demonstrated that the effect of solidification rate depending on particle size on segregation and constitution of the phases in the gas-atomized β-solidifying γ-TiAl alloy powder. In addition, the understanding of microstructural evolution provides guidance for such rapid solidification manufacturing processes.

Acknowledgments

This work was supported by a Grant-in-Aid for Transformative Research Area A (21H05198, 22H05288) and Scientific Research (22H01812 and 23H00235) from the Japan Society for the Promotion of Science (JSPS), and CREST-Nanomechanics: Elucidation of macroscale mechanical properties based on understanding nanoscale dynamics of innovative mechanical materials (Grant Number: JPMJCR2194) from the Japan Science and Technology Agency (JST).

References

1) J.C. Williams, and E.A.S. Jr: Acta Mater. **51** (2003) 5775–5799.

2) M. Peters, J. Kumpfert, C.H. Ward, and C. Leyens: Adv. Eng. Mater. **5** (2003) 419–427.

3) B.P. Bewlay, S. Nag, A. Suzuki, and M.J. Weimer: Mater. A. T. High. Temp. **33** (2016) 549–559.

4) S. Lee, M.-S. Shin, and Y.-J. Kim: Metall. Mater. Trans. B **51** (2020) 861–869.

5) M. Thomas, J.L. Raviart, and F. Popoff: Intermetallics **13** (2005) 944–951.

6) T. Voisin, J.P. Monchoux, L. Durand, N. Karnatak, M. Thomas, and A. Couret: Adv. Eng. Mater. **17** (2015) 1408–1413.

7) K. Cho, H. Kawabata, T. Hayashi, H.Y. Yasuda, H. Nakashima, M. Takeyama, and T. Nakano: Addit. Manuf. **46** (2021) 102091.

8) K. Cho, R. Kobayashi, J.Y. Oh, H.Y. Yasuda, M. Todai, T. Nakano, A. Ikeda, M. Ueda, and M.

Takeyama: Intermetallics **95** (2018) 1–10.

9) H. Amano, T. Ishimoto, R. Suganuma, K. Aiba, S.H. Sun, R. Ozasa, and T. Nakano: Addit. Manuf. **48** (2021) 102444.

10) N. Ikeo, T. Matsumi, T. Ishimoto, R. Ozasa, A. Matsugaki, T. Matsuzaka, O. Gokcekaya, Y. Takigawa, and T. Nakano: Crystals **11** (2021) 1074.

11) N. Ikeo, H. Fukuda, A. Matsugaki, T. Inoue, A. Serizawa, T. Matsuzaka, T. Ishimoto, R. Ozasa, O. Gokcekaya, and T. Nakano: Crystals **11** (2021) 959.

12) J. Lehtonen, Y. Ge, N. Ciftci, O. Heczko, V. Uhlenwinkel, and S.P. Hannula: J. Alloy. Compd. **827** (2020) 154142.

13) R. Gerling, H. Clemens, and F.P. Schimansky: Adv. Eng. Mater. **6** (2004) 23–38.

14) G.A. Rao, M. Srinivas, and D.S. Sarma: Mater. Sci. Eng. A **435–436** (2006) 84–99.

15) A. Martín, C.M. Cepeda-Jiménez, and M.T. Pérez-Prado: Adv. Eng. Mater. **22** (2020) 1900594.

16) O. Gokcekaya, T. Ishimoto, T. Todo, P. Wang, and T. Nakano: Addit. Manuf. Lett. **1** (2021) 100016.

17) C. Pleass, and S. Jothi: Addit. Manuf. **24** (2018)

419–431.

18) X. Ding, L. Zhang, J. He, F. Zhang, X. Feng, H. Nan, J. Lin, and Y.W. Kim: J. Alloy. Compd. **809** (2019) 151862.

19) E. Schwaighofer, H. Clemens, S. Mayer, J. Lindemann, J. Klose, W. Smarsly, and V. Güther: Intermetallics **44** (2014) 128–140.

20) M. Kastenhuber, T. Klein, B. Rashkova, I. Weißensteiner, H. Clemens, and S. Mayer: Intermetallics **91** (2017) 100–109.

21) S. Mayer, M. Petersmann, F.D. Fischer, H. Clemens, T. Waitz, and T. Antretter, Acta Mater. **115** (2016) 242–249.

22) M. Takeyama, and S. Kobayashi: Intermetallics **13** (2005) 993–999.

23) T. DebRoy, H.L. Wei, J.S. Zuback, T. Mukherjee, J.W. Elmer, J.O. Milewski, A.M. Beese, A. Wilson-Heid, A. De, and W. Zhang: Prog. Mater. Sci. **92** (2018) 112–224.

24) S.H. Sun, K. Hagihara, T. Ishimoto, R. Suganuma, Y.F. Xue, and T. Nakano: Addit. Manuf. **47** (2021)102329.

25) Z.C. Cordero, H.M. Meyer, P. Nandwana, and

R.R. Dehoff: Acta Mater. **124** (2017) 437–445.

26) D.Y. Yang, S. Guo, H.X. Peng, F.Y. Cao, N. Liu, and J.F. Sun: Intermetallics **61** (2015) 72–79.

27) D.Y. Yang, H.X. Peng, Y.Q. Fu, F.Y. Cao, Z.L. Ning, S. Guo, Y.D. Jia, N. Liu, and J.F. Sun: Nanosci. Nanotechnol. Lett. **7** (2015) 603–610.

28) X. Zhang, C. Li, M. Wu, Z. Ye, Q. Wang, and J. Gu: Acta Mater. **227** (2022) 117718.

29) O. Gokcekaya, T. Ishimoto, Y. Nishikawa, Y.S. Kim, A. Matsugaki, R. Ozasa, M. Weinmann, C. Schnitter, M. Stenzel, H.S. Kim, Y. Miyabayashi, and T. Nakano: Mater. Res. Lett. **11** (2023) 274–280.

30) T. Ishimoto, R. Ozasa, K. Nakano, M. Weinmann, C. Schnitter, M. Stenzel, A. Matsugaki, T. Nagase, T. Matsuzaka, M. Todai, H.S. Kim, and T. Nakano: Scr. Mater. **194** (2021) 113658.

31) D. Laipple, A. Stark, F.P. Schimansky, B. Schwebke, F. Pyczak, and A. Schreyer: Key Eng. Mat. **704** (2016) 214–222.

32) V. Tong, S. Joseph, A.K. Ackerman, D. Dye, and T.B. Britton: J. Microsc. **267** (2017) 318–329.

33) X. Zhang, B. Mao, L. Mushongera, J. Kundin,

and Y. Liao: Mater. Des. **201** (2021) 109501.

34) T.B. Massalski: Metall. Mater. Trans. A **33** (2002) 2277-2283.

35) R. Ozasa, A. Matsugaki, T. Ishimoto, and T. Nakano: Mater. Trans. **64** (2023) 31–36.

Captions list

Table 1 The detailed particle size distributions of the investigated powder.

Table 2 Characteristics of powder shape for investigated powder after gas-atomization.

Fig. 1 Particle size distribution for the small and large powders. Gray and black bars represent the data for small and large powder, respectively.

Fig. 2 Powder shape analysis. FE-SEM images of powder for (a) small and (b) large powders at low magnification and the insets are taken at high magnification. (c) Two-dimensional projection images of small powders, (d) particle size distribution based on area equivalent diameter analyzed by the obtained image analysis, and (e) the relation between area equivalent diameter and circularity.

Fig. 3 Highly magnified FE-SEM images as an example of powder particles. The image shows (a) dendritic surface, and (b) dendritic morphology in the cross-section, respectively.

Fig. 4 Chemical distribution in the cross-section of powder by SEM-EDS analysis for (a) small and (b) large size powder.

Fig. 5 (a) Compare the XRD pattern of the small and large powder and phase maps of the (b) small and (c) large powders, respectively.

Fig. 6 (a) The phase map of the small size of the powder with the β and α_2 phase constitution. (b) detailed SEM-BSE image denoted in (a) with the black dotted square.

Fig. 7 (a) Schematic phase diagrams of the β-solidifying γ-TiAl alloy systems over the interested composition range in this study. (b-d) illustrates the subsequent microstructural evolution according to the solidification process.

Table 1 The detailed particle size distributions of the investigated powder.

Measured characteristics	Small	Large
D_{10} [μm]	17.3	59.7
D_{50} [μm]	36.0	78.7
D_{90} [μm]	60.4	105.0
$(D_{90} - D_{10}) / D_{50}$	1.12	0.57

Table 2 Characteristics of powder shape for investigated powder after gas-atomization.

Measured characteristics	
Powder area [μm^2]	941.0 ± 691.7
Powder perimeter [µm]	110.0 ± 43.8
Maximum feret diameter [µm]	37.4 ± 14.4
Minimum feret diameter [µm]	28.3 ± 12.7
Area equivalent diameter [µm]	32.2 ± 12.8
Circularity	0.92 ± 0.6

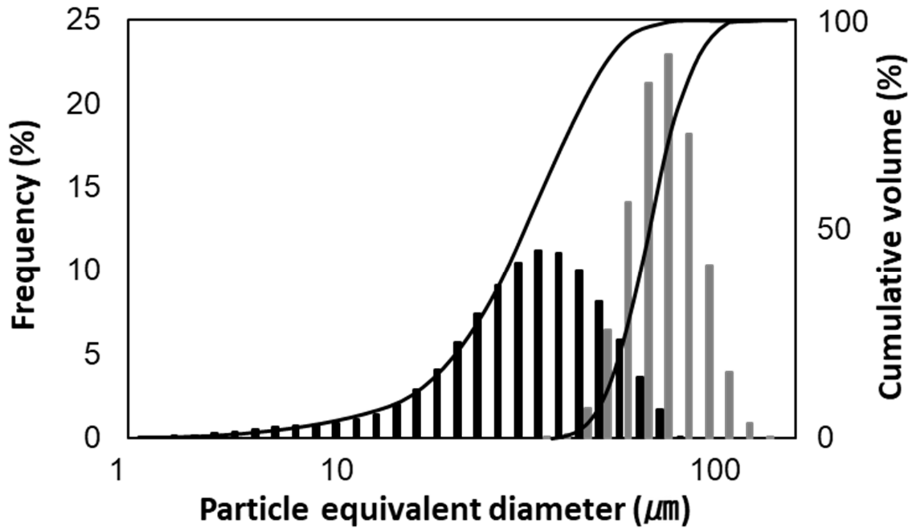

Fig. 1 Particle size distribution for the small and large powders. Gray and black bars represent the data for small and large powder, respectively.

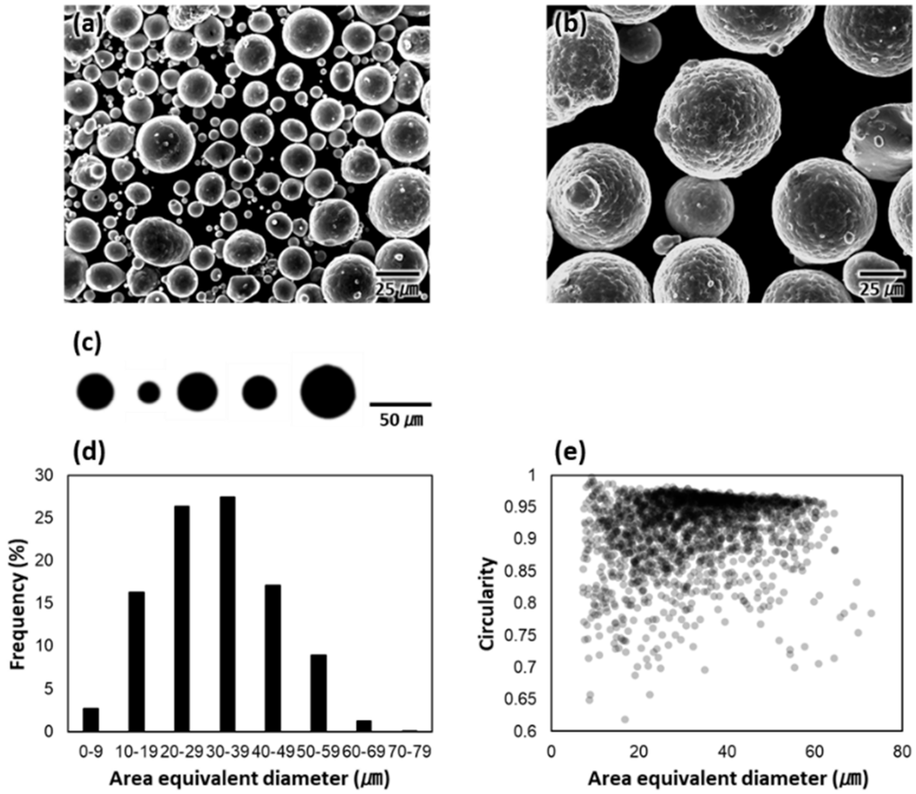

Fig. 2 Powder shape analysis. FE-SEM images of powder for (a) small and (b) large powders at low magnification and the insets are taken at high magnification. (c) Two-dimensional projection images of small powders, (d) particle size distribution based on area equivalent diameter analyzed by the obtained image analysis, and (e) the relation between area equivalent diameter and circularity.

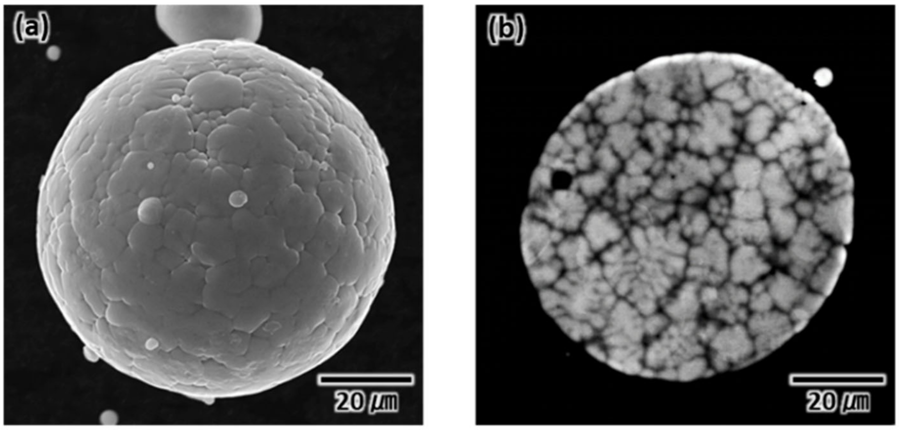

Fig. 3 Highly magnified FE-SEM images as an example of powder particles. The image shows (a) dendritic surface, and (b) dendritic morphology in the cross-section, respectively.

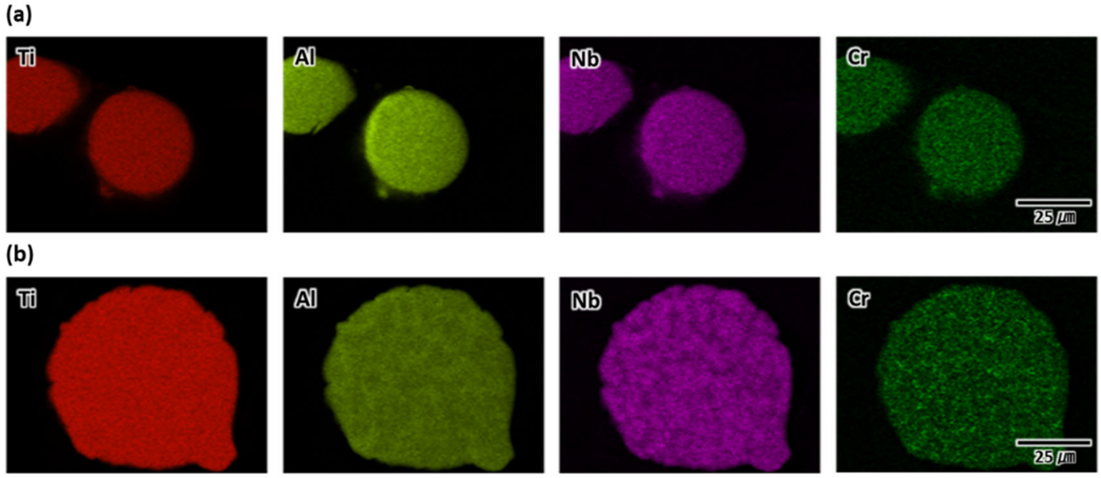

Fig. 4 Chemical distribution in the cross-section of powder by SEM-EDS analysis for (a) small and (b) large size powder.

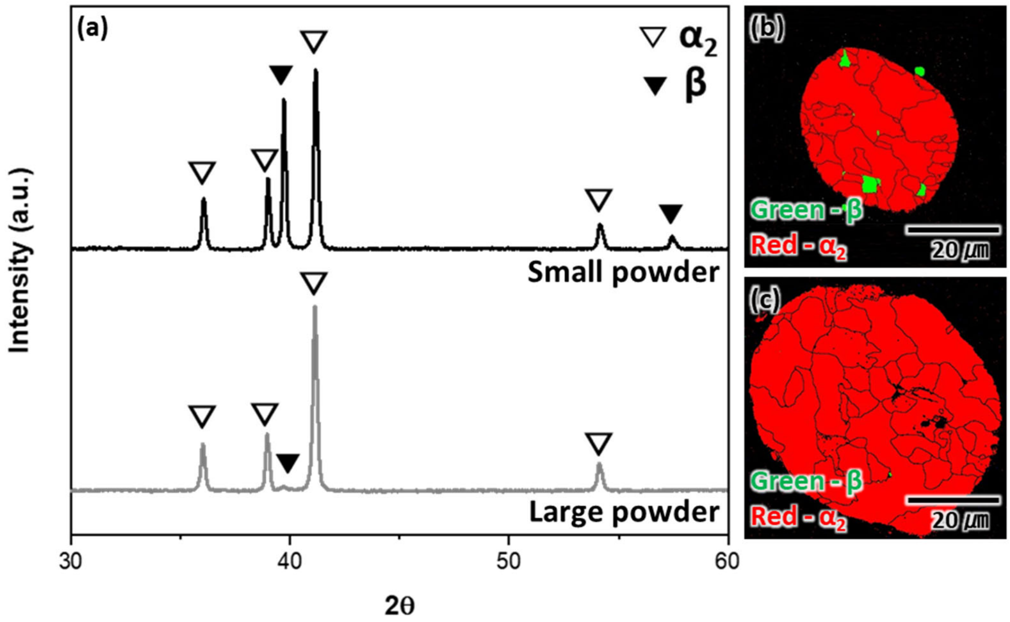

Fig. 5 (a) Compare the XRD pattern of the small and large powder and phase maps of the (b) small and (c) large powders, respectively.

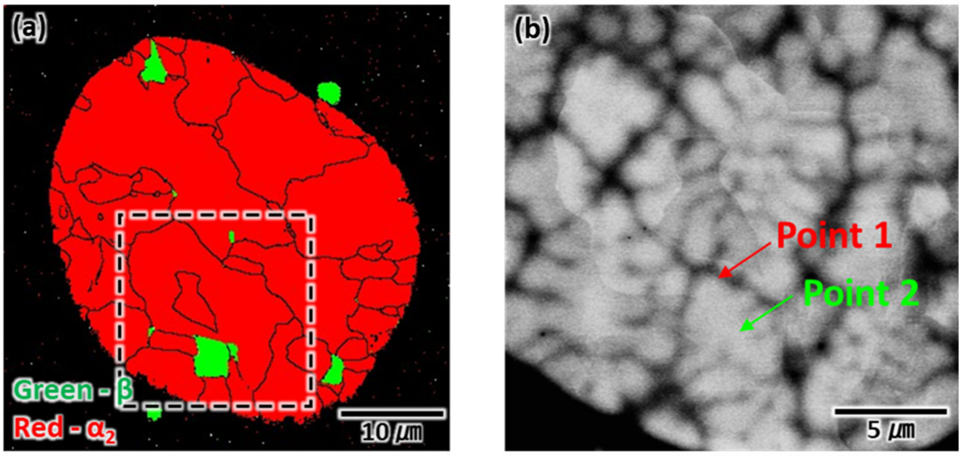

Fig. 6 (a) The phase map of the small size of the powder with the β and α_2 phase constitution. (b) detailed SEM-BSE image denoted in (a) with the black dotted square.

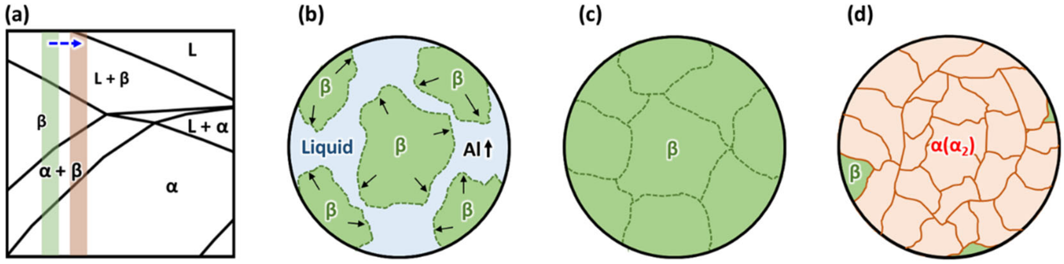

Fig. 7 (a) Schematic phase diagrams of the β-solidifying γ-TiAl alloy systems over the interested composition range in this study. (b-d) illustrates the subsequent microstructural evolution according to the solidification process.